



Open Research Online

The Open University's repository of research publications
and other research outputs

Lunar samples record an impact 4.2 billion years ago that may have formed the Serenitatis Basin

Journal Item

How to cite:

Cernok, Ana; White, Lee F.; Anand, Mahesh; Tait, Kimberly T.; Darling, James R.; Whitehouse, Martin; Miljković, Katarina; Lemelin, Myriam; Reddy, Steven M.; Fougereuse, Denis; Rickard, William D. A.; Saxey, David W. and Ghent, Rebecca (2021). Lunar samples record an impact 4.2 billion years ago that may have formed the Serenitatis Basin. *Communications Earth & Environment*, 2(1), article no. 120.

For guidance on citations see [FAQs](#).

© 2021 The Authors



<https://creativecommons.org/licenses/by/4.0/>

Version: Version of Record












Link(s) to article on publisher's website:

<http://dx.doi.org/doi:10.1038/s43247-021-00181-z>

Copyright and Moral Rights for the articles on this site are retained by the individual authors and/or other copyright owners. For more information on Open Research Online's data [policy](#) on reuse of materials please consult the policies page.

oro.open.ac.uk

Lunar samples record an impact 4.2 billion years ago that may have formed the Serenitatis Basin

Ana Černok ^{1,2,3}, Lee F. White^{1,2,3}, Mahesh Anand ^{1,4}, Kimberly T. Tait ^{2,3}, James R. Darling ⁵, Martin Whitehouse ⁶, Katarina Miljković ⁷, Myriam Lemelin ⁸, Steven M. Reddy ^{9,10}, Denis Fougerouse ^{9,10}, William D. A. Rickard⁹, David W. Saxey ⁹ & Rebecca Ghent³

Impact cratering on the Moon and the derived size-frequency distribution functions of lunar impact craters are used to determine the ages of unsampled planetary surfaces across the Solar System. Radiometric dating of lunar samples provides an absolute age baseline, however, crater-chronology functions for the Moon remain poorly constrained for ages beyond 3.9 billion years. Here we present U–Pb geochronology of phosphate minerals within shocked lunar norites of a boulder from the Apollo 17 Station 8. These minerals record an older impact event around 4.2 billion years ago, and a younger disturbance at around 0.5 billion years ago. Based on nanoscale observations using atom probe tomography, lunar cratering records, and impact simulations, we ascribe the older event to the formation of the large Serenitatis Basin and the younger possibly to that of the Dawes crater. This suggests the Serenitatis Basin formed unrelated to or in the early stages of a protracted Late Heavy Bombardment.

¹School of Physical Sciences, The Open University, Milton Keynes, UK. ²Centre for Applied Planetary Mineralogy, Department of Natural History, Royal Ontario Museum, Toronto, ON, Canada. ³Department of Earth Sciences, University of Toronto, Toronto, ON, Canada. ⁴Department of Earth Sciences, The Natural History Museum, London, UK. ⁵University of Portsmouth, School of Earth & Environmental Sciences, Portsmouth, UK. ⁶Department of Geosciences, Swedish Museum of Natural History, Stockholm, Sweden. ⁷Space Science and Technology Centre, School of Earth and Planetary Sciences, Curtin University, Perth, WA, Australia. ⁸Département de Géomatique appliquée, Université de Sherbrooke, Sherbrooke, QC, Canada. ⁹Geoscience Atom Probe, John de Laeter Centre, Curtin University, Perth, WA, Australia. ¹⁰School of Earth and Planetary Sciences, Curtin University, Perth, WA, Australia. ✉email: ana.cernok@open.ac.uk

One of the outstanding questions in planetary science is the exact timing and duration of impact bombardment to the inner Solar System, including the purported Late Heavy Bombardment (LHB)^{1–11}. Direct constraints on the timing and duration of the impact bombardment can be provided by absolute ages of the most ancient lunar surfaces and basins⁷. Closely linked to this topic is the timing of formation of the Serenitatis Basin—one of the largest and the oldest impact basins on the Moon (Supplementary Fig. 1). Whether the Serenitatis Basin formed during the classical LHB has been a matter of debates for decades^{2,7,12–15}. Essentially, an ancient age of Serenitatis Basin would support the idea of protracted bombardment period^{2,4,5,11,16–19}, and cast into doubt the onset and duration of the classical, spike-like LHB⁵. Recent arguments have revived the interpretations of its ancient (~4.1–4.3 billion years, Gyr) age^{2,12,13}. However, no lunar sample has ever been identified, which could provide a direct support to this hypothesis. Most Apollo 17 samples are impact-melt breccias initially identified as originating from the Serenitatis Basin²⁰, but more recent studies^{12,21} have associated these breccias with Imbrium formation (~3.8–3.9 Gyr).

As the oldest components of the lunar crust, the highlands samples record the earliest lunar evolution and cratering history. The Apollo 17 samples, 78235 and 78236, are intrusive highlands rocks, compositionally defined as norites of the so-called *magnesian-suite* that were emplaced very early during lunar crust formation (~4.3–4.4 Gyr)²². The norites were sampled at Station 8 in Taurus-Littrow Valley (Supplementary Fig. 1), at the base of the Sculptured Hills on the southeastern edge of the Serenitatis Basin²³, and are some of the most extensively studied samples from the Moon. These, alongside norite samples 78238, 78255 and 78256 were chipped off a ~0.5 m boulder with a coarse-grained, cumulus texture, indicative of origin within deep-crustal settings²³. However, because the boulder was partially coated in glassy impact melt, it contained pervasive melt veins, and the rock's overall composition could not be readily linked to the geology of the immediate surroundings, it was proposed that the boulder was excavated from depth by a large basin-forming impact event^{23,24}. The texture and appearance of the minerals imply severe impact-related deformation in these rocks that are commonly referred to as 'the most heavily shocked' rocks of the Apollo collection^{25,26}.

The complex impact history and transportation of the samples are reflected in their geochronology. A number of studies utilising most of the available geochronometers reveal ages of these norites spanning from 4.43 to 4.11 Gyr^{22,27–31}. Phosphate minerals, apatite [Ca₅(PO₄)₃(F, Cl, OH)] and merrillite [Y- and REE-rich Ca₉Na(Fe,Mg)(PO₄)₇] are common accessory minerals in 78235 and 78236 norites. These minerals are established as highly sensitive impact chronometers^{21,32,33} as a result of their moderate temperature of closure to solid state Pb diffusion (~450 °C, depending on the grain size and cooling rates)³⁴ and well-constrained response to shock metamorphism³⁵. Here we present the first in situ U–Pb and Pb–Pb ages of highly shocked apatite and merrillite in 78235 and 78236, using secondary ion mass spectrometry (SIMS). This is complemented by new Pb–Pb ages of baddeleyite (ZrO₂) that help refine the original crystallisation age of these samples. We further employ atom-probe tomography (APT) to assess the nanostructure and chemical composition of dated apatite. Using numerical iSALE-2D impact simulation and Kaguya Multiband (MI) remote sensing data, we suggest a possible provenance of the Station 8 norites.

Results and discussion

Timing of norite crystallisation and the radiogenic ages of baddeleyite. Petrological and mineralogical investigations of

78235 and 78236 samples infer the boulder was formed during one single crystallisation event²³. The timing of crystallisation is best obtained by robust and refractory geochronometers, which are unlikely to reset their radiogenic clock during later impact and heating events (e.g. Pb–Pb or Sm–Nd). The baddeleyite grains analysed in this study yield ²⁰⁷Pb/²⁰⁶Pb ages of 4346 ± 18 and 4323 ± 14 Myr (Supplementary Table 2). Ages previously obtained for samples from the Station 8 boulder range from 4430 ± 50 to 4110 ± 20 Myr^{22,27–30,36} (note older decay constants in refs. 28,30). Crystallisation ages of 4430 ± 50 Myr obtained by Sm–Nd³⁰ and U–Pb³¹ have been superseded by more recent studies. For instance, the Pb–Pb isochron ages of 4333 ± 59 Myr²⁷ obtained on the whole rock and major mineral separates in the norites, concordant with a Sm–Nd isochron of 4334 ± 37 Myr^{27,36} are interpreted to best reflect the crystallisation age of the rock. Formerly reported SIMS Pb–Pb ages of baddeleyite (~4260 Myr³⁷) and zircon (4220 ± 40 Myr³⁷) are within the range of those more recently obtained for baddeleyite and zirconolite (from 4347 ± 22 to 4220 ± 21 Myr³⁸), interpreted to represent variable age-resetting of ~4320 Myr magmatic baddeleyite by a ~4200 Myr impact event³⁸. Hence, the two baddeleyite Pb–Pb ages obtained in this study, 4346 ± 18 and 4323 ± 14 Myr, are consistent with crystallisation ages reported so far.

Radiogenic ages of the phosphates. Comparison of the two independent ²⁰⁶Pb/²³⁸U and ²⁰⁷Pb/²³⁵U geochronometers from shocked phosphates (Fig. 1) define an upper concordant intercept of 4210 ± 14 Myr and a discordant array extending down to a lower concordant intercept of 504 ± 24 Myr (all reported uncertainties are 2σ; Supplementary Table 2). The upper intercept age is younger than the crystallisation age of the host rock as recorded by baddeleyite Pb–Pb ages obtained in this study (4346 ± 18 and 4323 ± 14 Myr) and crystallisation ages^{22,27,36–38} reported so far, indicating the loss of Pb from the phosphate minerals ~130 Myr after crystallisation. Detailed petrographic record of the norites provides compelling evidence that at least one major shock-deformation event reached peak pressures in excess of 50 GPa^{26,30,35}. To account for cross-cutting relationships between fractures, impact-melt veins, diaplectic plagioclase glass and melted plagioclase^{23,25} it was suggested that the rock underwent

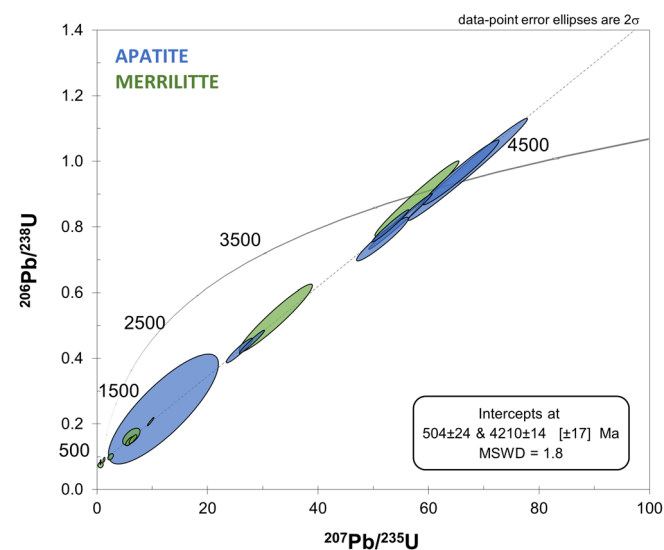


Fig. 1 Wetherill concordia diagram of absolute phosphate ages. U–Pb isotopic composition in eight apatite (blue) and ten merrillite (green) grains from 78235 and 78236 norites. The upper and the lower intercept are annotated. Isotopic ratios are reported in Supplementary Table 2.

one or two disturbance events at 4.11 ± 0.02 Gyr²⁸ and/or at 4.27 ± 0.02 Gyr³⁰. However, this was not confirmed by more recent ⁴⁰Ar–³⁹Ar studies that include new K-decay constant²⁹. Microtextural inspection of shocked phosphates, and associated baddeleyite and plagioclase phases recently revealed severe crystal-plastic deformation, and notably, recrystallisation as a result of the major shock deformation³⁵. Based on these observations, it can be ruled out that any of these minerals crystallised fresh during the major shock event. Instead, their microtextural characteristics indicate that the primary igneous minerals underwent significant modification during a major, high-temperature impact, which is consistent with them recording the time of this event at ~ 4200 Myr.

The ⁴⁰Ar–³⁹Ar isotopic system can also record relatively low-temperature resetting³⁹ and diffusive loss of radiogenic ⁴⁰Ar induced by shock heating²⁹. Most recent bulk rock ⁴⁰Ar–³⁹Ar analyses of shocked norite 78235 yield well-defined age plateaus at 4188 ± 13 Myr²⁹, indistinguishable from previously obtained ⁴⁰Ar–³⁹Ar ages^{28,30} (once corrected for monitor age and the K-decay constant). This age is interpreted as recording a thermal resetting, but the study excluded the possibility for a complete resetting of the Ar ages due to the lack of well-developed annealing features in major minerals (at $> \mu\text{m}$ scale, see Supplementary Discussion 2.2)²⁹. Nevertheless, this age is within uncertainty of the youngest zircon, baddeleyite and zirconolite ages reported from these samples^{37,38}, as well as the upper intercept age of the phosphates (4210 ± 14 Myr) obtained in this study. This evidence provides independent support for a long-standing hypothesis that a large, basin-forming impact event at ~ 4200 Myr exhumed the norites from their original emplacement depths^{23,29,30}, and caused pervasive shock deformation to these rocks.

The lower intercept age of 504 ± 24 Myr indicates a second significant disturbance of Pb. This disturbance is not reported in any other isotopic chronometers, including low-temperature chronometers such as ⁴⁰Ar–³⁹Ar dating of feldspars. It is therefore unlikely that this event represents the major impact responsible for the ubiquitous impact deformation features recorded in the norites. Hence, a different process needs to account for this disturbance. Based on our current understanding of the thermal evolution of the lunar interior, it is unlikely that the thermal event at ~ 504 Myr was caused by volcanism or a similar indigenous process, as these have not been identified in any other samples or near the Apollo 17 landing site. This young event is also not concordant with the cosmic ray exposure (CRE) age of the shocked norites (~ 260 Myr²⁹), which reflects the length of direct exposure of the sample on the lunar surface. To assess the likely mechanisms responsible for this young resetting event we first characterised the nanoscale features of the phosphate minerals and then use these to constrain the timescale and temperatures over which Pb loss must have occurred.

Boulder-size characteristics and phosphate nanoscale grain size constraints. Assumptions of the impact origin were earlier based on glass veins, glass coating and surface striations on the boulder 8. The size of the boulder seems unlikely to be a clast from the breccias sampled at the North and South Massifs; not only is it larger than most clasts observed in the breccias, but there is no trace of matrix adhering to the boulder. Additionally, the norite boulder provides the only large example of non-mare material recognised by the crew at Station 8²³. All these features indicate that the boulder itself was a fractured but largely intact ~ 0.5 m ejecta block^{23,40}, setting important size constraints for its ejection history.

Electron Backscatter Diffraction (EBSD) analyses of the phosphates showed a broad change in orientation variation across the apatite grains, i.e. up to $\sim 25^\circ$ of total misorientation³⁵ (Supplementary Fig. 2), reflecting the likely shock-induced bending of the lattice due to the ubiquitous deformation caused by the most pervasive impact they record (~ 4.2 Gyr impact). In other words, the EBSD reveals small grains separated by grain boundaries with low misorientation angles from the adjunct grains that progressively change their orientation. However, no obvious signs of recrystallisation are visible at the EBSD scale. The nanostructure of the deformed apatite (Supplementary Fig. 2) was investigated using 3D compositional and spatial imaging by APT⁴¹, to look for evidence of apatite recrystallisation and trace element mobility at the nanoscale (Supplementary Method 1.1). The APT revealed the nanoscale structure comprises ~ 10 nm and larger polygonal grains that are separated by grain boundaries meeting at triple-junctions (Fig. 2 and Supplementary Movies 1, 2). This annealed appearance indicates a significant component of grain boundary migration, with the recrystallised grains that appear to inherit the original orientation of the crystal-plastically deformed apatite. We interpret the size and shape of the polygonal grains to result from shock-induced recrystallisation by grain nucleation and short-duration annealing accommodated by grain boundary migration, a mechanism that has been observed as very efficient in resetting Pb⁴². The broad microtextural context of the entire phosphate grain and associated minerals³⁵ (Supplementary Fig. 2), coupled with its geochronology imply that this recrystallisation was shock-induced during the major impact event at ~ 4200 Myr.

As evident in the SIMS data, most Pb was lost during the ~ 504 Myr event. Considering the nanoscale structure of apatite, we interpret that its fine-grained nature was critical for enabling rapid Pb diffusion out of the apatite grains to the grain boundaries. Using the diffusion parameters for apatite³⁴ and

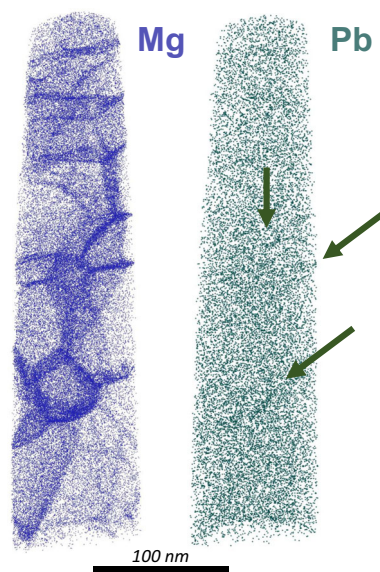


Fig. 2 Atom-probe tomography analysis of a shocked lunar apatite. An APT microtip (M3) of 78236 apatite that shows severe crystal-plastic deformation (shown in Supplementary Fig. 2). Polygonal grains that can be recognised by Mg decoration of grain boundaries indicate recrystallisation at the nanoscale. Minor Pb is trapped within the grain boundaries along with Mg (arrows indicating Pb enrichment). Exact Pb concentrations are shown in Supplementary Fig. 2. See Supplementary Movie 1 for a 3D animation of this entire microtip and Supplementary Movie 2 for the shape of the grain boundaries.

the observed grain size range, we calculated the fractional Pb loss due to a short-duration thermal pulse (70 min–1 day; likely cooling rate of a ~0.5 m radius boulder on the lunar surface that has an initial temperature of ~700 °C) over a range of temperatures (Supplementary Discussion 2.1 and Supplementary Fig. 4). This modelling suggests that in order to diffuse a substantial amount of Pb out of the smallest grain (~10 nm) and initiate an effective resetting (50% or higher), the peak temperature during the ~504 Myr event had to be in excess of 550 °C. Complete Pb loss of ~20 nm diameter grains would take place at temperatures of ~700 °C (or higher for larger grains). A range of grain sizes led to variable amounts of Pb diffusion, and this could explain why analyses fall on the mixing line between the ~504 and ~4200 Myr concordant points. Although most Pb was lost along the boundaries that acted as fast diffusion pathways, a minor, residual Pb component that was trapped within the grain boundaries represents a snapshot of the final stages of Pb loss (Fig. 2 and Supplementary Fig. 2). The trapped Pb potentially contributes to the mixing line between the ~504 and ~4200 Myr events. The rapid heating and the temperature range inferred by the nanostructure of apatite suggest that the Pb disturbance was caused by a minor, secondary impact ~504 Myr ago, which does not seem to have disturbed other geochronometers (e.g. Ar–Ar, Supplementary Discussion 2.2). We further investigate geographical distribution of the nearby lunar craters as potential sources.

Dawes as a possible source crater. It was recognised many years ago that Station 8 shocked norites are likely to be samples of the deeper lunar crust and hence, it was argued that they must have been exposed at the surface as a result of a major, basin-forming event (e.g. Imbrium, Serenitatis)^{14,20,23,40}. However, the surface setting of the boulder suggests that its last movement was not by a large (basin-forming) impact, and that its former residing place was not too distant²³. This observation led other researchers to propose that the final source crater is small (minimum ~1.5 km diameter) and in the vicinity (up to ~60 km) of the Apollo 17 landing site. Supported by compositional maps derived from the Moon Mineralogy Mapper (M³) data, a potential source crater is suggested from the Sculptured Hills, but no firm links have been established^{40,43}. However, ballistic emplacement of the boulder to

its resting position does not reconcile the evidence of the micrometeorite impact pits that cover the entire boulder surface²³. The pits imply that the boulder was rolled over the surface, possibly when a landslide ~260 Myr ago, corresponding to the sample's CRE age²⁹, excavated it from near-surface depths and rolled it down to the bottom of the valley. To find the source crater of the boulder, from which it was ejected to the position prior to the possible landslide, we can utilise the younger age of Pb isotopic resetting in apatite (~504 Myr) as a temporal constraint on the timing of this young impact. A recent database of lunar craters, documenting <1 Gyr old craters with diameter equal to or greater than 10 km⁴⁴, reveals that Dawes is the closest crater to the Apollo 17 landing site that has a formation age (454⁺¹⁷¹₋₁₃₂ Myr; 95% credible intervals on the joint lunar and terrestrial regression⁴⁴) in the range of the young event recorded by phosphates (504 ± 24 Myr). This ~18 km-diameter crater is located ~140 km away on the southeastern rim of the Serenitatis Basin. No other candidates were identified in or near the Sculptured Hills while other craters of <1 Ga are not suitable (e.g. Proclus 253 Myr old, ~500 km away).

To test whether the norites could have originated from the Dawes crater, we investigated mineral composition of the crater floor, walls and surrounding lithology by looking into compositional remote sensing data from the Kaguya Multiband Imager (MI). The Kaguya-derived mineral maps are quantitative maps at a spatial resolution of ~62 m/pixel, obtained by radiative transfer modelling of the four major lunar minerals: plagioclase, olivine, low-Ca pyroxene (orthopyroxene, or LCP), high-Ca pyroxene (clinopyroxene, or HCP), assuming a fixed magnesium number (Mg# = 65)^{45,46}. We used derived maps to look for pixels matching mineral composition of the norites^{30,47–49}, allowing for 7 wt.% of error on the mineral abundance maps. At least three pixels, corresponding to ~11,500 m², at the bottom of the Dawes crater (Fig. 3) were found to entirely match these compositional constraints of investigated norites, revealing spectra that are best fitted with model abundances of 6–7 wt.% olivine, 47–52 wt.% orthopyroxene, 6–7 wt.% clinopyroxene and 35–41 wt.% plagioclase (Fig. 3). These three pixels coincide with rocky floor observed by the Narrow Angle Camera (NAC) and a peak in topographic SLDEM2015 data and could present a central uplift of the Dawes crater (Fig. 3 and Supplementary Fig. 10). Importantly, only if we look for pixels that have a broader and

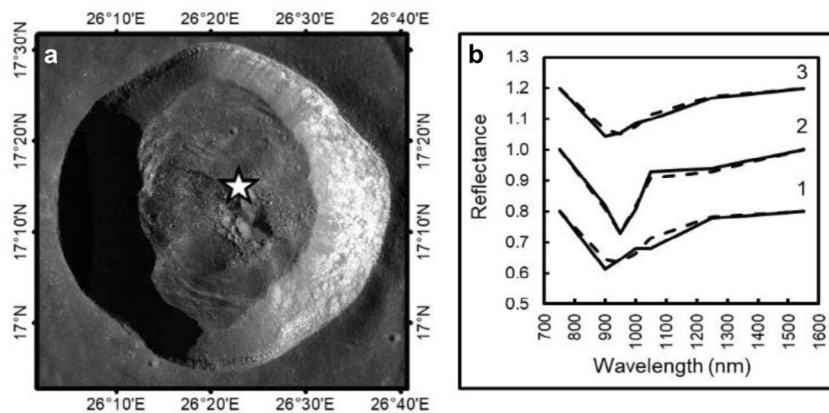


Fig. 3 Kaguya MI spectral analysis of Dawes crater. **a** Dawes crater as seen by the Lunar Reconnaissance Orbiter Narrow Angle Camera (low-Sun controlled mosaic). The star denotes the location of the three pixels for which modelled spectra closely resemble Multiband Imager spectra and are within the same compositional range as the 78235 and 78236 samples. **b** The Multiband Imager continuum removed spectra for these three pixels (solid lines) along with their best modelled spectral fit (dashed lines). The spectra have been offset for clarity. Spectra 1 is modelled as 35 wt.% plagioclase, 52 wt.% low-calcium pyroxene, 7 wt.% high-calcium pyroxene and 7 wt.% olivine. Spectra 2 is modelled as 41 wt.% plagioclase, 47 wt.% low-calcium pyroxene, 6 wt.% high-calcium pyroxene and 6 wt.% olivine. Spectra 3 is modelled as 40 wt.% plagioclase, 48 wt.% low-calcium pyroxene, 6 wt.% high-calcium pyroxene and 6 wt.% olivine.

less-matching compositional range (33–61% orthopyroxene and 32–55% plagioclase), we find pixels also outside the central peak of Dawes crater—a total of 34,619 such pixels concentrated on the central peak, on the southern crater wall and in proximal ejecta (Supplementary Figs. 10 and 11a). Similar broad-range composition can be observed all the way to the Apollo 17 site (Supplementary Fig. 11b), but we have not inspected this entire area for close-matched composition, as no age-matching craters of appropriate size were found there. Nevertheless, the broad-range composition suggests that Dawes crater is a non-unique location in terms of orthopyroxene-plagioclase-rich rocks being exposed on the surface.

Dawes crater ejecta simulations. After confirming mineralogical evidence on the floor of the Dawes crater to contain rocks of comparable composition to the Apollo 17 shocked norites, a question arises whether noritic material could have been ballistically transported ~140 km away. An additional complexity is that the ejecta must have been sourced from the noritic crustal bedrock underlying the 300 m thick mare basalt⁵⁰ within which Dawes formed. To test this scenario, we used Numerical iSALE-2D impact simulation of the formation of the Dawes-size crater (Supplementary Method 1.2 and Supplementary Discussion 2.3). The simulations show that a portion of ejecta that originated from the crust (set as dunite in the simulations) beneath basalt, reached up to almost 2 km depth (Fig. 4a). This modelling indicates that the entire ejecta blanket originating from underneath the mare layer experienced temperatures up to 700 °C (Fig. 4b, 1000 K). About 20% of the entire ballistic ejecta was moving at speeds that can result in landing 140 km away and most of this fast ejecta formed 30 s after the impact (Fig. 4c). Any later ejecta would have been too slow to reach the Apollo 17 site. In summary, the simulations confirm that significant portion of ejecta formed by Dawes crater could have landed in the Taurus-Littrow valley, after being exposed up to 700 °C, as required by the Pb-diffusion calculations.

However, iSALE code cannot distinguish individual blocks nor predict the survivability of an individual ~0.5 m boulder. Although Dawes crater ejecta landing 140 km away can be considered as distal, which refers to patchy and discontinued materials, it remains unknown whether the initial size of the boulder was ~0.5 m or larger. Petrographical observations suggest the boulder was unlikely to be a part of a larger brecciated ejecta block²³. Nevertheless, it may be speculated—based on the fact that some surface areas of the boulder were not covered by glass

—it was not a boulder of this size throughout its transportation history but a part of a larger glass and vein rich norite with similar composition and texture. Ultimately, the boulder was likely covered by surface material upon landing, as inferred by the CRE ages²⁹ that imply the boulder had not been exposed on the surface between the ~504 and ~260 Myr events. Finally, the boulder was brought to the surface through a landslide ~260 Myr ago which could have transported it in its final size (no other blocks were recognised nearby) to the valley. Considering these size uncertainties, we explore different block sizes when constraining cooling of the boulder (Supplementary Discussion 2.1). However, it is very unlikely that the landing caused additional shock-related modifications to the ejecta block regardless of its initial size, as demonstrated by a proxy 25-m block, which was mostly exposed to very low pressures and temperatures upon landing (Supplementary Discussion 2.3 and Supplementary Fig. 9).

Implication for the age of Serenitatis. Cumulus texture of Station 8 shocked norites has been interpreted to reflect deep-crustal origin of these rocks that were brought to the surface by a basin-forming impact needed to excavate them from deep-crustal environment. Since the Apollo 17 mission, the impact in question has been associated with either Imbrium or Serenitatis basin-forming events^{14,29,51}. Station 8 was primarily planned with the aim to obtain material from the Sculptured Hills, interpreted as an ejecta from the Serenitatis Basin^{14,51}. Nevertheless, most other Apollo 17 samples are impact-melt breccias initially identified as originating from the Serenitatis Basin, and the associated impact-resetting ages suggested this basin to be of ~3.87 Gyr age²⁰. More recent terrain¹² and geochronological²¹ studies have associated these breccias with Imbrium formation. A possible link of Apollo 17 impact-melt breccias with Imbrium is further established through a record of similar ~3.8–3.9 Gyr resetting ages in many other Apollo 14, 15 and 16 samples (refs. 29,40 and refs. therein). This age has been now widely accepted and interpreted as the formation of the Imbrium Basin^{12,29,32,52}. Importantly, this interpretation is consistent with the simulated results that predict a high fraction of Imbrium melt at Apollo 14–17 sites, but reduced presence of Serenitatis melt due to impact gardening^{53,54}. In contrast, any possibility of Imbrian deformation in 78235 and 78236, which are samples of crustal rocks different from impact-melt breccias, is excluded by the lack of ~3.8–3.9 Gyr events in the sensitive U–Pb record of the shocked phosphates studied here, or other geochronometers previously reported²⁹. We argue

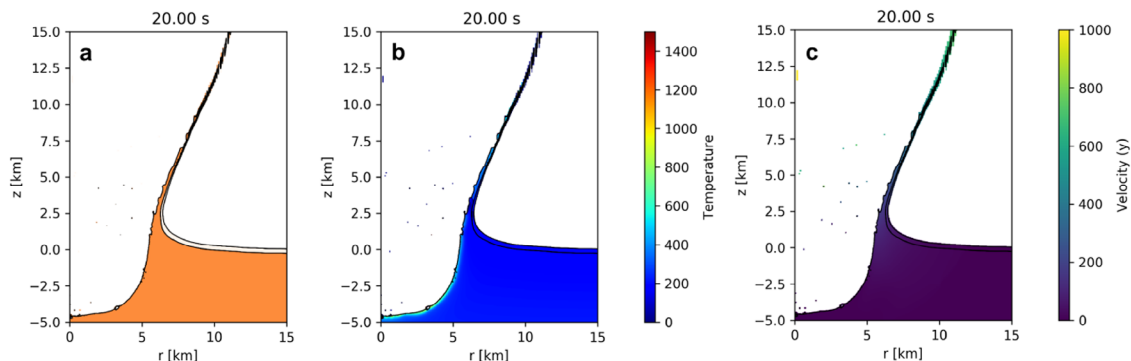


Fig. 4 2D Numerical simulation of the Dawes crater formation. Snapshots are taken during the early crater excavation phase (20 s after impact) that includes the ejecta creation. The black line separates the 300-m-thick mare basalt layer from the underlying crust. The material plot (a) indicates some material was excavated deeper than the mare layer at this time. The temperature plot (b) shows that all ejecta composed of the underlying crust layer experienced $T < 1000$ K at this time. Velocity plot (c) shows the vertical component of velocity vector (y), indicating that the bulk of the ejecta is moving at < 600 m/s, with the maximum at ~1000 m/s. Safe estimate suggest about 20% of the ejecta coming from the underlying crust to have sufficient launch speeds to reach the landing site.

that the major, basin-forming event which excavated Station 8 norites from the deeper lunar crust and caused the shock-induced deformation of the ancient age (~4.2 Gyr) recorded by the phosphates is representative of the formation of Serenitatis. A formerly reported ^{40}Ar – ^{39}Ar age of ~4.2 Gyr for these rocks was not interpreted as impact-resetting because the samples were considered to show limited petrologic features indicative of thermal annealing representative of a basin-forming impact. However, our microstructural studies of minerals and apatite nanoscale features provide robust evidence of such deformation. An impact-resetting age of ~4.2 Gyr has been recorded in other Apollo samples, too, for example in Apollo 14¹⁸ and Apollo 16^{17,29,55} impact-melt breccias. A possible link of some of the Apollo 16 breccias¹⁷ to Nectaris Basin was suggested based on geographical vicinity, but it was disputed for other Apollo 16 samples based on bulk geochemical properties⁵⁵. Whether the 4.2 Gyr impact age recorded by Apollo 16 and 14 samples is related to the Serenitatis Basin is out of the scope of this study. Nevertheless, we can exclude a possibility that Station 8 shocked norites could have been transported from as far as Nectaris Basin based on textural and temperature constraints.

Multiple impacts and relocation histories of rock samples on lunar surface are possible⁵³ and have been employed to explain complex geochronology of other Apollo samples⁵⁶. As demonstrated by numerical modelling, a crater of a size comparable to that of Dawes could have excavated the Serenitatis rim, transporting the ejected material to the Taurus-Littrow Valley without substantial heating above 700 °C. The remote sensing mineralogical data is strongly suggestive of the presence of noritic material at the bottom of Dawes crater that formed ~453.9 (+117.1/–132.2) Myr ago. If a more local source crater of the norites than Dawes is envisioned in the Sculptured Hills region and within the 60 km surroundings^{40,43}, we point out that this entire area is within the peak ring region of the Serenitatis Basin (Supplementary Fig. 1), which further strengthens the relation of the ~4.2 Gyr event to the deformation caused by Serenitatis Basin formation.

Our findings unequivocally contribute to the growing arguments for increased impacting rate on the Moon much before ~3.8–3.9 Gyr^{4,5,11,17,19,29,52,55,57,58} and provide a rare evidence for samples recording >3.8–3.9 Gyr impact events⁵⁴. We provide a sample-based evidence in form of microstructurally-constrained ~4.2 Gyr impact-resetting phosphate age in support of revived arguments for the ancient (>3.9 Gyr) age of the Serenitatis Basin^{1,2,12}. Importantly, our data provide robust evidence that the phosphate U–Pb geochronometer has an immense potential to be utilised as a sensitive recorder of shock events in planetary materials. We argue that the Serenitatis Basin, like South Pole Aitken Basin⁴, was formed either unrelated to the highly-debated spike-like LHB⁵, or early on in the protracted bombardment period^{2,4,5,16}, warranting a re-evaluation of the earliest lunar crater chronology.

Methods

Secondary ion mass spectrometry for U–Pb and Pb–Pb analysis. Eight apatite, ten merrillite and two baddeleyite grains were analysed within two thin sections (78235,43 and 78236,44). Thin sections were coated with a ~30 nm layer of gold on the top of the carbon coat, to reduce gold accumulation in the cracks. U–Pb isotopic measurements were performed using a CAMECA ims1280 ion microprobe at the NordSIMS facility, located at the Swedish Museum of Natural History (Stockholm), closely following previously reported protocols for Ca-phosphate analyses^{21,32,52}. We targeted apatite and merrillite grains that are associated with them, to ensure a larger dataset. A duoplasmatron-generated primary beam of O_2^- ions with 1.7–5.3 nA current was used for spot analyses of 7 or 10 μm , selected using apertures to match the grain size. The nominal mass resolution ($M/\Delta M$) used of ~5400 was sufficient to resolve Pb peaks from molecular interferences. Data reduction was performed using in-house developed software at NordSIMS and the Excel add-in Isoplot (v. 4.15⁵⁹). Non-radiogenic (common) Pb monitored using

^{204}Pb was assumed to be the result of terrestrial contamination of the section and was corrected using the Stacey and Kramers⁶⁰ model for present-day terrestrial Pb isotopic composition. Sample Pb/U ratios were calibrated against the NW1 ~1160 Ma apatite standard (~100 ppm uranium, $^{206}\text{Pb}/^{238}\text{U} = 0.197152$ and $^{206}\text{Pb}/^{204}\text{Pb} > 500^{61}$) using a power law relationship between measured $^{206}\text{Pb}^*/\text{U}$ and UO/U ratios. Additional uncertainty is associated to differences in crystal chemistry and crystal structure of the standard and the unknown grains, variations in instrumental conditions between analysis of standards on an epoxy block and unknown samples on the thin sections, as well as the surface conditions related to the fact that the analysed grain experienced shock deformation. In particular, the lack of a suitable merrillite standard, requires these analyses to be corrected with the apatite standard, which may not adequately correct for the matrix effects on U/Pb ratios. In order to test the matrix effect on merrillite, we plotted common Pb-corrected apatite and merrillite data separately as well as combining all common Pb-uncorrected data on an inverse concordia diagram, which showed that the effect, if any, is negligible (Supplementary Fig. 3). In contrast to U/Pb, $^{207}\text{Pb}/^{206}\text{Pb}$ are unaffected by these standard-sample discrepancies⁶² and are, after common Pb correction, considered to provide the best estimate of the sample ages for the concordant grains. Pb isotope analyses of baddeleyite were conducted using a 1 nA duoplasmatron-generated O_2^- beam of ca. 7 nA, but using multicollector detection in four low-noise ion-counting electron multipliers at a mass resolution ($M/\Delta M$) of 4860, similar to conditions reported elsewhere⁵⁷. Oxygen flooding of the sample chamber was used to enhance secondary Pb ion yields from baddeleyite by a factor of 7. Detector gains were calibrated using BCR-2g basaltic glass and common Pb-corrected $^{207}\text{Pb}/^{206}\text{Pb}$ ratios assume minor terrestrial contamination of the thin section, as for apatite and merrillite. All reported phosphate and baddeleyite ages assume the decay constants recommendations of Steiger and Jäger⁶³ and are reported with 2 σ errors. All ratios are reported in Supplementary Table 2, Supplementary Data 2 and in a repository⁶⁴.

Atom-probe tomography for nanoscale Pb distribution. Sample preparation for atom-probe tomography was performed using a TESCAN LYRA3 Ga⁺ focused ion beam scanning electron microscope (FIB-SEM) located in the John de Laeter Centre (JdLC) at Curtin University, Australia. Site specific targeting of apatite was performed using methods outline in⁶⁵, followed by a lift-out procedure commonly used for non-conducting materials⁶⁶. An area of interest in the form of a ~2 × 25 μm rectangle (Supplementary Fig. 2) was initially covered by Pt. The wedge of the grain directly below the Pt-area was cut out on three sides using a coarse milling approach under accelerated voltage of 30 kV. The wedge was fixed to an in situ micromanipulator by depositing Pt, before the final edge was cut free. APT sample preparation involved further slicing of the wedge into 1–2 μm wide segments that were sequentially mounted to Si tips in an array, using Pt-deposition. Finally, applying annular milling with decreasingly smaller inner diameter, the segments were shaped into conical APT microtips. Final polishing at reduced beam conditions of 20 pA and at 2 kV ascertained removal of the beam-damaged, amorphized surface implanted with Ga⁺ ions of the tips. Exact locations of the APT microtips referred are reported in the Supplementary Fig. 2.

Atom-probe analyses of the FIB-prepared microtips were conducted on a CAMECA local-electrode atom probe (LEAP 4000X HR) at the Geoscience Atom Probe Facility, Curtin University. APT of apatite utilises laser-assisted field evaporation of needle-shaped specimens coupled with time-of-flight mass spectrometry. Evaporated ions are accelerated by the field, pass through a reflectron system and hit a position-sensitive detector, and the time between laser pulse and detection yields the mass/charge ratio of the ionic species via time-of-flight mass spectrometry. Instrument and acquisition parameters for this study are provided in Supplementary Table 1. Microtips are inserted into ultra-high vacuum (~10^{–11} Torr), cooled down to 69 K, and a high voltage applied (typically 4–14 kV). Field evaporation and ionisation is stimulated with an ultraviolet laser ($\lambda = 355 \text{ nm}$) that is focused on the specimen apex and pulsed at frequency of 125–200 kHz, with an energy of 250–400 pJ per pulse. These conditions are similar to those previously applied in an APT study of apatite⁶⁷. As the radius of the microtip increased with the ongoing evaporation, the voltage was gradually increased to automatically maintain an ion detection rate of ~0.006–0.008 ions per pulse. After completing a flight path of ~382 mm, ions are detected on the position-sensitive detector and their mass/charge ratio is determined from their time-of-flight. The data is represented as a mass/charge spectra, and the chemical identities of peaks are identified and ranged in Supplementary Fig. 2. Together with the related spatial information from the ion detection, this allows for a 3D reconstruction of the positions and chemical identities of atoms within the specimen, achieving approximately nanometre resolution (in x – y – z space) and a mass resolving power $M/\Delta M$ of ~800. The 3D reconstruction of ionic species was based on using the voltage curve to estimate the evolution of the tip radius during each experiment. In case of the M3 experiment, SEM images acquired before and after the experiment were used to constrain the spatial reconstruction parameters, following the approach of Saxey et al.⁶⁸. Processing and peak ranging were carried out using the CAMECA integrated visualisation and analysis software (IVAS, v. 3.8.0).

iSALE-2D numerical impact modelling. The numerical impact formation of the Serenitatis basin and the Dawes crater were made in the iSALE-2D shock physics

hydrocode, the code typically used for simulating cratering process in geologic materials available at <https://isale-code.github.io/>. Numerical impact modelling of the Serenitatis basin formation was based on previous studies (Supplementary Method 1.2)^{69,70}. All input parameters are provided in Supplementary Data 1 and in a repository⁶⁴. We adopted values for the Serenitatis crustal thinning diameter of 600 km, crustal thickening of 850 km, and the coupling parameter of 427⁶⁹ as well as tentative value of 416 km for the inner ring diameter and 923 km for the main rim⁷¹. Using the basin scaling laws from ref. ⁶⁹, and assuming that the vertical impact speed at the Moon was 17 km/s⁷², the projectile diameter was set to 80 km in diameter. The GRAIL gravity estimated an average crustal thickness at Serenitatis to be 26 ± 8 km, therefore we adopted 30 km as the pre-impact crustal thickness. The outcome from the model is shown in Supplementary Figures 6 and 7, for the two ages during the lunar thermal evolution. Both simulation outcomes agree with the GRAIL-gravity observations of the Serenitatis basin. The Dawes crater is ~18 km in diameter, and it has a morphology between simple and complex crater (Supplementary Method 1.2 and Supplementary Discussion 2.3). The vertical impact was made using 600-m diameter projectile made of dunite, impacting at 17 km/s. The target rock is set to be a 300 m thick layer of mare basalt, an average thickness reported in that region^{50,73}, overlaying dunitic rock underneath to represent the peak ring material from the Serenitatis basin (Supplementary Figs. 6–8). More details on the numerical impact modelling of the Dawes crater can be found in Supplementary Methods (1.2) and Discussion (2.3).

Remote sensing using Kaguya spectral images. The Kaguya Multiband Imager acquired data in 9 ultraviolet-visible (UVVIS) to near-infrared (NIR) spectral bands (415, 750, 900, 950, 1001, 1000, 1050, 1250, 1550 nm). The instrument provided a spatial resolution of ~20 m per pixel for the first five spectral bands (UVVIS, 415–1001 nm), and ~62 m per pixel for the last four (NIR, 1000–1550 nm) at the nominal altitude of 100 km^{74,75}. We used the IDL 5.5.3 software (L3Harris geospatial <https://www.l3harrisgeospatial.com/Software-Technology/IDL/>) to run the mineral mapping algorithm and the ArcGIS 10.8.1 software suite (ESRI <https://www.esri.com/en-us/arcgis/about-arcgis/overview>) to produce the maps. In this study, all maps were created (Fig. 3 and Supplementary Figs. 10 and 11) using Multiband Imager reflectance data corrected for the shading effects of topography (MAP 03 processing level) available online via the SELENE data archive at <http://l2db.selene.darts.isas.jaxa.jp/index.html.en>). We downsampled the UVVIS data to the same spatial resolution as the NIR (~62 m/pixel) so that we could work with 9 spectral bands with matching spatial resolution. We also corrected systematic differences in the reflectance spectra between the first five spectral bands (UVVIS data) and the last four (NIR data), as they were obtained by two different detectors. We then used radiative transfer modelling, constrained by the spectrally determined abundance of FeO, to estimate the abundance of plagioclase, low-calcium pyroxene, high-calcium pyroxene and olivine in each pixel (Supplementary Fig. 10). These mineral maps incorporate improved optical constants and space weathering modelling, increased spatial resolution and a better correction of the reflectance data (corrected for the shading effects of topography)^{45,46}. The method is explained in detail by refs. ^{45,46}. We then looked for pixels that have a composition that corresponds to the sample's composition⁷⁶ ± 7 wt.%, which correspond to the mineral maps error. Previous studies have reported a composition as follows: 40–48 wt.% plagioclase, 40–54 wt.% low-calcium pyroxene and 0–1 wt.% high-calcium pyroxene (summarised in ref. ⁷⁶). We thus looked for pixels that have 32–55 wt.% plagioclase, 33–61 wt.% low-calcium pyroxene, 0–8 wt.% high-calcium pyroxene and 0–7 wt.% olivine. The MI spectrum of three pixels closely match the modelled spectra within this range of compositions. Unfortunately, no Spectral Profiler orbit is available across the area of interest to provide hyperspectral data as a confirmation of the composition. All remote sensing data generated for this study are presented in Supplementary Figs. 10 and 11 and in the online repository⁷⁷.

Data availability

Correspondence and material requests should be addressed to Ana Ćernok at ana.cernok@gmail.com or ana.cernok@open.ac.uk. The supporting iSALE modelling input files and run parameters are provided as Supplementary Data 1 and in the online repository⁶⁴. Remote sensing data generated for this study using Multiband Imager reflectance data (available online via the SELENE data archive at <http://l2db.selene.darts.isas.jaxa.jp/index.html.en>) are stored in the online repository⁷⁷. The geochronological data that support the findings of this study are available in the Supplementary Table 2, Supplementary Data 2 and in the online repository⁶⁴. Supplementary Movies 1 and 2 show atom-probe tomography data and are also provided in the online repository⁶⁴.

Code availability

The numerical impact formation of the Serenitatis Basin and the Dawes crater were made in the iSALE-2D available at <https://isale-code.github.io/>. We used the IDL 5.5.3 software (L3Harris geospatial <https://www.l3harrisgeospatial.com/Software-Technology/IDL/>) to run the mineral mapping algorithm and the ArcGIS 10.8.1 software suite (ESRI <https://www.esri.com/en-us/arcgis/about-arcgis/overview>) to produce the maps. Supplementary Information is available for this paper.

Received: 21 October 2020; Accepted: 6 May 2021;

Published online: 09 June 2021

References

- Fassett, C. I. & Minton, D. A. Impact bombardment of the terrestrial planets and the early history of the Solar system. *Nat. Geosci.* **6**, 520–524 (2013).
- Fassett, C. I. et al. Lunar impact basins: stratigraphy, sequence and ages from superposed impact crater populations measured from Lunar Orbiter Laser Altimeter (LOLA) data. *J. Geophys. Res. Planets* **117**, 1–13 (2012).
- Hartmann, W. K. The giant impact hypothesis: past, present (and future?). *Philos. Trans. Math. Phys. Eng. Sci.* **372**, 1–13 (2014).
- Morbidelli, A., Marchi, S., Bottke, W. F. & Kring, D. A. A sawtooth-like timeline for the first billion years of lunar bombardment. *Earth Planet. Sci. Lett.* **355–356**, 144–151 (2012).
- Marchi, S., Bottke, W. F., Kring, D. A. & Morbidelli, A. The onset of the lunar cataclysm as recorded in its ancient crater populations. *Earth Planet. Sci. Lett.* **325–326**, 27–38 (2012).
- Kring, D. A. & Cohen, B. A. Cataclysmic bombardment throughout the inner solar system 3.9–4.0 Ga. *J. Geophys. Res. Planets* **107**, 4–1 (2002).
- Bottke, W. F. & Norman, M. D. The late heavy bombardment. *Annu. Rev. Earth Planet. Sci.* **45**, 619–647 (2017).
- Stöffler, D. et al. Cratering history and lunar chronology. *Rev. Mineral. Geochem.* **60**, 519–596 (2006).
- Tera, F., Papanastassiou, D. A. & Wasserburg, G. J. Isotopic evidence for a terminal lunar cataclysm. *Earth Planet. Sci. Lett.* **22**, 1–21 (1974).
- Wetherill, G. W. Late heavy bombardment of the moon and terrestrial planets. *Proc. Lunar Sci. Conf.* **6**, 1539–1561 (1975).
- Mojzsis, S. J., Brasser, R., Kelly, N. M., Abramov, O. & Werner, S. C. Onset of giant planet migration before 4480 million years ago. *Astrophys. J.* **881**, 44 (2019).
- Spudis, P. D., Wilhelms, D. E. & Robinson, M. S. The Sculptured Hills of the Taurus Highlands: Implications for the relative age of Serenitatis, basin chronologies and the cratering history of the Moon. *J. Geophys. Res. Planets* **116**, E00H03 (2011).
- Orgel, C. et al. Ancient bombardment of the inner solar system: reinvestigation of the “fingerprints” of different impactor populations on the lunar surface. *J. Geophys. Res. Planets* **123**, 748–762 (2018).
- Head, J. W. Serenitatis multi-ringed basin: Regional geology and basin ring interpretation. *Moon Planets* **21**, 439–462 (1979).
- Evans, A. J. et al. Reexamination of early lunar chronology with GRAIL data: terranes, basins, and impact fluxes. *J. Geophys. Res. Planets* **123**, 1596–1617 (2018).
- Fassett, C. I. Analysis of impact crater populations and the geochronology of planetary surfaces in the inner solar system. *J. Geophys. Res. Planets* **121**, 1900–1926 (2016).
- Norman, M. D. & Nemchin, A. A 4.2 billion year old impact basin on the Moon: U–Pb dating of zirconolite and apatite in lunar melt rock 67955. *Earth Planet. Sci. Lett.* **388**, 387–398 (2014).
- Hopkins, M. D. & Mojzsis, S. J. A protracted timeline for lunar bombardment from mineral chemistry, Ti thermometry and U–Pb geochronology of Apollo 14 melt breccia zircons. *Contrib. Mineral. Petrol.* **169**, 30 (2015).
- Crow, C. A., McKeegan, K. D. & Moser, D. E. Coordinated U–Pb geochronology, trace element, Ti-in-zircon thermometry and microstructural analysis of Apollo zircons. *Geochim. Cosmochim. Acta* **202**, 264–284 (2017).
- Stöffler, D. Cratering history and lunar chronology. *Rev. Mineral. Geochem.* **60**, 519–596 (2006).
- Thiessen, F., Nemchin, A. A., Snape, J. F., Whitehouse, M. J. & Bellucci, J. J. Impact history of the Apollo 17 landing site revealed by U–Pb SIMS ages. *Meteorit. Planet. Sci.* **52**, 584–611 (2017).
- Carlson, R. W., Borg, L. E., Gaffney, A. M. & Boyet, M. Rb–Sr, Sm–Nd and Lu–Hf isotope systematics of the lunar Mg-suite: the age of the lunar crust and its relation to the time of Moon formation. *Philos. Transact. A Math. Phys. Eng. Sci.* **372**, 1–37 (2014).
- Jackson, E. D., Sutton, R. L. & Wilshire, H. G. Structure and petrology of a cumulus norite boulder sampled by Apollo 17 in Taurus-Littrow Valley, the Moon. *Geol. Soc. Am. Bull.* **86**, 433–442 (1975).
- Das, J. P., Baldwin, S. L. & Delano, J. W. 40Ar/39Ar and cosmic ray exposure ages of plagioclase-rich lithic fragments from Apollo 17 regolith 78461. *Earth Planets Space* **68**, 11 (2016).
- Sclar, C. B. & Bauer, J. F. Shock-induced subsolidus reduction-decomposition of orthopyroxene and shock induced melting of norite 78235. In *Proceedings, 6th Lunar Science Conference* 799–820 (1975).
- El Goresy, A., Engelhardt, W., von Arndt, J. & Manglier, J. Shocked norite 78235: primary textures and shock features. In *Proceedings, 7th Lunar Science Conference* 239–241 (1976).

27. Edmunson, J., Borg, L. E., Nyquist, L. E. & Asmerom, Y. A combined Sm–Nd, Rb–Sr, and U–Pb isotopic study of Mg–suite norite 78238: further evidence for early differentiation of the Moon. *Geochim. Cosmochim. Acta* **73**, 514–527 (2009).
28. Aeschlimann, U. et al. On the age of Cumulate Norite 78236: a 39Ar–40Ar Study. *Lunar Planet. Sci. Conf.* **13**, 1–2 (1982).
29. Fernandes, V. A., Fritz, J., Weiss, B. P., Garrick-Bethell, I. & Shuster, D. L. The bombardment history of the Moon as recorded by 40Ar–39Ar chronology. *Meteorit. Planet. Sci.* **48**, 241–269 (2013).
30. Nyquist, L. E. et al. A comparative Rb–Sr, sm–nd and K–Ar study of shocked norite 78236: evidence of slow cooling in the lunar crust? *Lunar Planet. Sci. Conf.* **12**, 67–97 (1981).
31. Premo, W. R. & Tatsumoto, M. U–Th–Pb isotopic systematics of lunar norite 78235. *Proc. Lunar Planet. Sci. Conf.* **21**, 89–100 (1991).
32. Snape, J. F. et al. Phosphate ages in Apollo 14 breccias: resolving multiple impact events with high precision U–Pb SIMS analyses. *Geochim. Cosmochim. Acta* **174**, 13–29 (2016).
33. McGregor, M., McFarlane, C. R. M. & Spray, J. G. In situ LA-ICP-MS apatite and zircon U–Pb geochronology of the Nicholson Lake impact structure, Canada: shock and related thermal effects. *Earth Planet. Sci. Lett.* **504**, 185–197 (2018).
34. Cherniak, D. J., Lanford, W. A. & Ryerson, F. J. Lead diffusion in apatite and zircon using ion implantation and Rutherford Backscattering techniques. *Geochim. Cosmochim. Acta* **55**, 1663–1673 (1991).
35. Černok, A., White, L. F., Darling, J., Dunlop, J. & Anand, M. Shock-induced microtextures in lunar apatite and merrillite. *Meteorit. Planet. Sci.* **54**, 1262–1282 (2019).
36. Carlson, R. W. & Lugmair, G. W. Time and duration of lunar highlands crust formation. *Earth Planet. Sci. Lett.* **52**, 227–238 (1981).
37. Hinthorne, J. R., Conrad, R. L. & Church, S. E. Lead-lead age and rare earth element determinations in Lunar Norite 78235. **8**, (1977).
38. Zhang, A. C. et al. SIMS Pb/Pb ages of Baddeleyite and Zirconolite in Apollo 17 Norite 78235: implications for shock histories of extraterrestrial rocks. In *43rd Lunar and Planetary Science Conference* 1036 (2012).
39. Cassata, W. S. & Renne, P. R. Systematic variations of argon diffusion in feldspars and implications for thermochronometry. *Geochim. Cosmochim. Acta* **112**, 251–287 (2013).
40. Schmitt, H. H. et al. Revisiting the field geology of Taurus–Littrow. *Icarus* **298**, 2–33 (2017).
41. Reddy, S. M. et al. Atom probe tomography: development and application to the geosciences. *Geostand. Geoanal. Res.* **44**, 5–50 (2020).
42. Erickson, T. M. et al. Deformed monazite yields high-temperature tectonic ages. *Geology* **43**, 383–386 (2015).
43. Petro, N. E., Klima, R. L. & Ostrach, L. R. Constraining the Origin of Apollo 17's Station 8 Boulder: implications for the origin of the sculptured hills and the Mg–Suite. In *46th Lunar and Planetary Science Conference* 2687 (2015).
44. Mazrouei, S., Ghent, R. R., Botke, W. F., Parker, A. H. & Gernon, T. M. Earth and Moon impact flux increased at the end of the Paleozoic. *Science* **363**, 253–257 (2019).
45. Lemelin, M., Lucey, P. G., Song, E. & Taylor, G. J. Lunar central peak mineralogy and iron content using the Kaguya Multiband Imager: Reassessment of the compositional structure of the lunar crust. *J. Geophys. Res. Planets* **120**, 869–887 (2015).
46. Lemelin, M. et al. The compositions of the lunar crust and upper mantle: Spectral analysis of the inner rings of lunar impact basins. *Planet. Space Sci.* **165**, 230–243 (2019).
47. Dymek, R. F., Albee, A. L. & Chodos, A. A. Comparative petrology of lunar cumulate rocks of possible primary origin: Dunite 72415, troctolite 76535, norite 78235, and anorthosite 62237. *Proc. Lunar Sci. Conf.* **6**, 301–341 (1975).
48. McCallum, I. S. & Mathez, E. A. Petrology of noritic cumulates and a partial melting model for the genesis of Fra Mauro basalts. *Proc. Lunar Sci. Conf.* **6**, 395–414 (1975).
49. James, O. B. & Flohr, M. K. Subdivision of the Mg–suite noritic rocks into Mg–gabbronorites and Mg–norites. *J. Geophys. Res. Solid Earth* **88**, A603–A614 (1983).
50. Oshigami, S. et al. Mare volcanism: Reinterpretation based on Kaguya Lunar Radar Sounding data. *J. Geophys. Res. Planets* <https://doi.org/10.1002/2013JE004568> (2014).
51. Head, J. W. Morphology and structure of the Taurus–Littrow Highlands (Apollo 17): evidence for their origin and evolution. *Moon* **9**, 355–395 (1974).
52. Nemchin, A. A. et al. The comparative behavior of apatite–zircon U–Pb systems in Apollo 14 breccias: Implications for the thermal history of the Fra Mauro Formation. *Meteorit. Planet. Sci.* **44**, 1717–1734 (2009).
53. Liu, T., Michael, G., Engelmann, J., Wünnemann, K. & Oberst, J. Regolith mixing by impacts: lateral diffusion of basin melt. *Icarus* **321**, 691–704 (2019).
54. Liu, T., Michael, G., Wünnemann, K., Becker, H. & Oberst, J. Lunar megaregolith mixing by impacts: Spatial diffusion of basin melt and its implications for sample interpretation. *Icarus* **339**, 113609 (2020).
55. Fischer-Gödde, M. & Becker, H. Osmium isotope and highly siderophile element constraints on ages and nature of meteoritic components in ancient lunar impact rocks. *Geochim. Cosmochim. Acta* **77**, 135–156 (2012).
56. Kelly, N. M., Flowers, R. M., Metcalf, J. R. & Mojzsis, S. J. Late accretion to the Moon recorded in zircon (U–Th)/He thermochronometry. *Earth Planet. Sci. Lett.* **482**, 222–235 (2018).
57. White, L. F. et al. Evidence of extensive lunar crust formation in impact melt sheets 4,330 Myr ago. *Nat. Astron.* 1–5 <https://doi.org/10.1038/s41550-020-1092-5> (2020).
58. Garrick-Bethell, I. et al. Troctolite 76535: a sample of the Moon's South Pole-Aitken basin? *Icarus* **338**, 113430 (2020).
59. Ludwig, K. R. *User's Manual for Isoplot 3.00: A Geochronological Toolkit for Microsoft Excel* (2003).
60. Stacey, J. S. & Kramers, J. D. Approximation of terrestrial lead isotope evolution by a two-stage model. *Earth Planet. Sci. Lett.* **26**, 207–221 (1975).
61. Li, Q.-L. et al. In-situ SIMS U–Pb dating of phanerozoic apatite with low U and high common Pb. *Gondwana Res.* **21**, 745–756 (2012).
62. Shimizu, N. & Hart, S. R. Isotope fractionation in secondary ion mass spectrometry. *J. Appl. Phys.* **53**, 1303–1311 (1982).
63. Steiger, R. H. & Jäger, E. Subcommittee on geochronology: Convention on the use of decay constants in geo- and cosmochronology. *Earth Planet. Sci. Lett.* **36**, 359–362 (1977).
64. Černok, A. Lunar samples record an impact 4.2 billion years ago that may have formed the Serenitatis Basin. <https://doi.org/10.5281/zenodo.4739278> (2021).
65. Rickard, W. D. A. et al. Novel applications of FIB-SEM-based ToF-SIMS in atom probe tomography workflows. *Microsc. Microanal.* 1–8 <https://doi.org/10.1017/S1431927620000136> (2020).
66. Thompson, K. et al. In situ site-specific specimen preparation for atom probe tomography. *Ultramicroscopy* **107**, 131–139 (2007).
67. Gordon, L. M., Tran, L. & Joester, D. Atom probe tomography of apatites and bone-type mineralized tissues. *ACS Nano* **6**, 10667–10675 (2012).
68. Saxey, D. W., Fougereuse, D., Rickard, W. D. A. & Reddy, S. M. Spatial reconstruction of atom probe data from zircon. *Microsc. Microanal.* **25**, 2536–2537 (2019).
69. Miljković, K. et al. Subsurface morphology and scaling of lunar impact basins. *J. Geophys. Res. Planets* **121**, 1695–1712 (2016).
70. Miljković, K. et al. Asymmetric distribution of lunar impact basins caused by variations in target properties. *Science* **342**, 724–726 (2013).
71. Neumann, G. A. et al. Lunar impact basins revealed by Gravity Recovery and Interior Laboratory measurements. *Sci. Adv.* **1**, e1500852 (2015).
72. Le Feuvre, M. & Wieczorek, M. A. Nonuniform cratering of the Moon and a revised crater chronology of the inner Solar System. *Icarus* **214**, 1–20 (2011).
73. Hiesinger, H., Jaumann, R., Neukum, G. & Head, J. W. Ages of mare basalts on the lunar nearside. *J. Geophys. Res. Planets* <https://doi.org/10.1029/2000JE001244> (2000).
74. Haruyama, J. et al. Global lunar-surface mapping experiment using the Lunar Imager/Spectrometer on SELENE. *Earth Planets Space* **60**, 243–255 (2008).
75. Ohtake, M. et al. Performance and scientific objectives of the SELENE (KAGUYA) Multiband Imager. *Earth Planets Space* **60**, 257–264 (2008).
76. Meyer, C. *Lunar Sample Compendium*. <https://curator.jsc.nasa.gov/lunar/lsc/> (2010).
77. Lemelin, M. Mineral maps for Dawes crater using Multiband Imager (MI_MAP_02) reflectance data. <https://doi.org/10.5281/zenodo.4560461> (2021).

Acknowledgements

M.A. and A.Č. thank NASA CAPTEM for the allocation of Apollo samples. A.Č. and M.A. acknowledge funding through MSCA fellowship to A.Č. from the EU's Horizon 2020 research and innovation programme (grant agreement no. 704696). A.Č., L.F.W. and K.T. acknowledge the Hatch Ltd. Fellowship and the CAMECA IVAS software license for data processing. The research was partially supported by a STFC grant to MA (#ST/P000657/1 and #ST/T000228/1). We are grateful for the constructive comments raised by three anonymous reviewers.

Author contributions

A.Č. and M.A. are responsible for study conceptualisation. L.F.W., K.T. and J.D. helped with further study design. A.Č. and M.W. carried out SIMS analyses and data reduction; A.Č., W.R., D. F., D.S. and S.R. carried out sample preparation and APT sample analyses. K.M. performed iSALE impact crater modelling; M.L. analysed Kaguya spectral images. R.G. contributed geological analysis, ages and uncertainties for Dawes crater. All co-authors were involved in data interpretation. A.Č. wrote the manuscript with contributions, review and editing by all co-authors.

Competing interests

The authors declare no competing interests.

Additional information

Supplementary information The online version contains supplementary material available at <https://doi.org/10.1038/s43247-021-00181-z>.

Correspondence and requests for materials should be addressed to A.Č.

Peer review information Primary handling editors: Joe Aslin, Heike Langenberg.

Reprints and permission information is available at <http://www.nature.com/reprints>

Publisher's note Springer Nature remains neutral with regard to jurisdictional claims in published maps and institutional affiliations.



Open Access This article is licensed under a Creative Commons Attribution 4.0 International License, which permits use, sharing, adaptation, distribution and reproduction in any medium or format, as long as you give appropriate credit to the original author(s) and the source, provide a link to the Creative Commons license, and indicate if changes were made. The images or other third party material in this article are included in the article's Creative Commons license, unless indicated otherwise in a credit line to the material. If material is not included in the article's Creative Commons license and your intended use is not permitted by statutory regulation or exceeds the permitted use, you will need to obtain permission directly from the copyright holder. To view a copy of this license, visit <http://creativecommons.org/licenses/by/4.0/>.

© The Author(s) 2021